Supporting Information

Synergistic carbon defects modulation in porous carbon nitride nanotubes for efficient photocatalytic hydrogen evolution

Bin Zhao [a, #], Beibei Zhang [b, #], Xing Liu [c], Zihao Mou [a], Baogang Wang [c], Zhijun Wang [a, *], Qingyuan Wang [a, *]

[a] Institute for Advanced Study, Chengdu University, 2025 Chengluo Avenue, Chengdu 610106, P. R. China.

[b] Institute of Fundamental and Frontier Sciences, University of Electronic Science and Technology of China, Chengdu 610054, P. R. China.

[c] College of Chemistry and Chemical Engineering, Southwest Petroleum University, No. 8 Xindu Avenue, Chengdu 610500, P. R. China.

[#] These authors contributed equally to this work.

Corresponding authors: Zhijun Wang, E-mail: wangzhijun@cdu.edu.cn; Qingyuan Wang, E-mail: wangqy@scu.edu.cn; Baogang Wang, E-mail: bgwang@swpu.edu.cn

1. Experimental section

Materials

Melamine ($C_3H_6N_6$), chloroplatinic acid ($H_2PtCl_6 \cdot 6H_2O$), sodium hydroxide (NaOH), and hydrochloric acid (HCl, 37%) were obtained from Sinopharm Chemical Reagent Ltd. (Shanghai, China). Deionized water with a resistivity of 18.25 $M\Omega \cdot cm^{-1}$ was used throughout the experiments. All reagents were analytical grade and used without further purification.

Synthesis of carbon vacancies modified carbon nitride nanotubes (C_v-TCN)

The C_3N_4 nanotubes were prepared by a dexterous template method. In a typical synthesis process, the cleaned eggshell was ground and passed through a 300-mesh sieve to remove large particles. Subsequently, the precipitate was filtered out after reflux at 80 ℃ in 0.1 M NaOH solution for 12 h, washed several times with deionized water and dehydrated. Next, 0.5 g of the treated eggshell and 2.0 g of melamine were put into 100 mL of water and stirred at 90 ℃ for 12 h. The solid is immediately filtered and washed with 50 mL of hot water. Subsequently, the dried mixed powder was placed in an Ar atmosphere and calcined at 550 ℃ for 4 h with a heating rate of 5 ℃/min. Finally, the calcined powder was treated with 1 M HCl to remove the template and wash and dry thoroughly to obtain the C_v-TCN samples.

Synthesis of bulk carbon nitride (BCN)

The BCN was synthesized according to the previous report with a slight

modification.[1] Briefly, Melamine (8 g) was heated to 550 °C for 4 h at the rate of 5 °C min^{-1} in a muffle furnace under an air atmosphere. Immediately, after cooling to room temperature, the BCN catalyst powder was obtained by grinding.

Characterization

Transmission electron microscopy (TEM) and Element distribution mapping (EDS) images were carried out on JEM-F200 (JEOL) with an acceleration voltage of 200 kV. Scanning electron microscope (SEM) images were obtained by JIB-4700F (JEOL) with an acceleration voltage of 10 kV. The structure of the samples was identified by X-ray diffraction analysis (XRD, D8 ADVANCE, Bruker) using Cu Kα radiation with a voltage of 40 kV as well as a current of 40 mA. The elemental composition was determined by X-ray photoelectron spectroscopy (XPS, PHI5000, ULVAC-PHI) with an excitation source of Al Kα (1486.6 eV), and all the spectra were calibrated by C 1s peak at 284.8 eV. Fourier transform infrared spectra (FT-IR) were tested on the Bruker V70 spectrometer with KBr pellets. UV-vis diffuse reflectance spectra were collected from a UV-Vis spectrophotometer (CARY300, Agilent) with $BaSO_4$ as the reference. The steady-state PL spectra and time-resolved PL (TRPL) were recorded from a Fluorophotometer (FluoTime 300, PicoQuant) with the 375 nm laser source. The specific surface areas were determined by a nitrogen adsorption instrument (QuadraSorb Station 4, Quantachrome), and the pore size distributions were determined by the Barrett-Joyner-Halenda (BJH) method. The hydrophilicity of samples was measured by a Contact Angle Measuring Instrument (DSA25E, Kruss) according to the

pendent drop method. Electron paramagnetic resonance (EPR) signals were recorded at room temperature (298 K) with a Bruker EMX microspectrometer. 20 mg of sample was filled in a sample tube and then transferred to the spectrometer under dark for measurement. The detailed spectrometer parameters were as follows: central field of 3200 G; sweep width of 5600.3 G; sweep time of 60.76 s; modulation amplitude of 8.0 G; modulation frequency of 100 kHz; microwave attention of 20 mW.

Photocatalytic H_2 evolution activity measurements

The photocatalytic reactions were carried out on an online photocatalytic analysis system (Labsolar-6A, PerfectLight) with a Pyrex top-irradiation reaction vessel. The H_2 production experiment was performed by dispersing 10 mg catalyst power in a 100 mL aqueous solution containing 10 mL methanol as the hole sacrificial reagent. Prior to measurement, 0.08 mL of H_2PtCl_6 solution (19.3 mM) was added to the system and illuminated for 30 min to allow the cocatalyst Pt to be photo-deposited onto the catalyst surface, and the 0.01 M of K_2HPO_4 was added to reaction cell to boosted the H_2 generation rate.[2] The temperature of the reaction system was maintained at 5 ℃ by the flow of cold water. Several times degassing was performed and a vacuum was maintained before being illuminated by a 300 W xenon lamp (PLS-SXE300, PerfectLight). During the reaction, the hydrogen production was quantified by online gas chromatography (GC7980, Techcomp).

Photoelectrochemical measurements

The photoelectrochemical experiments were conducted on an electrochemical workstation (CHI 760E) in 0.2 M Na_2SO_4 electrolyte (pH=6.8) under the irradiation provided by a 300 W solar simulator (Beijing Perfect Light Technology Co. Ltd.). In a typical three-electrode configuration, the sample photoelectrode (actual working area of 1 cm^2), Pt plate, and saturated Ag/AgCl (saturated KCl) were used as the working electrode, counter electrode, and reference electrode, respectively. The working electrode was prepared by drop-coating sample suspensions directly onto the pre-cleaned fluorine-doped tin oxide glass (FTO glass) surface. In detail, catalyst powder (5 mg) was dispersed into the mixed solution containing 0.75 mL of H_2O, 0.25 mL of isopropanol, and 20 μL of Nafion solution (5%). After sonication for 60 min, 50 μL of sample mixture was drop-coated onto the FTO glass and dried in an oven at 60 ℃ before being annealed in a tube furnace at 393 K for 120 min under Ar atmosphere. The electrode potentials of working electrodes were converted into reversible hydrogen electrode (RHE) potentials by the Nernst equation: $E_{RHE} = E_{Ag/AgCl} + E_{Ag/AgCl}^{\theta} + 0.0591 \times pH$ ($E_{Ag/AgCl}^{\theta} =$ 0.1976 V at 25 ℃). The electrochemical impedance spectroscopy (EIS) measurements were performed at a frequency range of 10^{-1} Hz to 10^5 Hz with a small AC amplitude of 10 mV under 1.23 V_{RHE} bias voltage. The *i-t* curves were recorded at 1.23 V_{RHE} with the light or dark conditions. The open-circuit potential profile was recorded between the light and dark transitions.

Computational details

All calculations were performed by using the Vienna Ab-initio Simulation Package with projector augmented wave pseudopotentials. The Perdew-Burke-Ernzerhof flavor of spin-polarized generalized gradient approximation was adopted for the exchange-correlation potential. In order to improve the description of the dispersion interaction between adsorbates and substrates, van der Waals correction was considered by using Grimme's D2 method. The optimized lattice parameter for buckling C_3N_4 was 6.99 Å. A 2 × 2 supercell of C_3N_4 with one cavity capturing a single Pt atom was used to model Pt@C_3N_4. A vacuum space of 15 Å was added in the z-direction to eliminate unphysical interaction between the replicas of periodic images. In all calculations, a plane wave cutoff energy of 500 eV was used. The Brillouin zone was sampled by a 3×3×1 k-mesh for the structure relaxation, respectively. The structure relaxations were fully relaxed until all residual forces below 0.02 eV/Å.

2. *Supplemental Figures and Discussions*

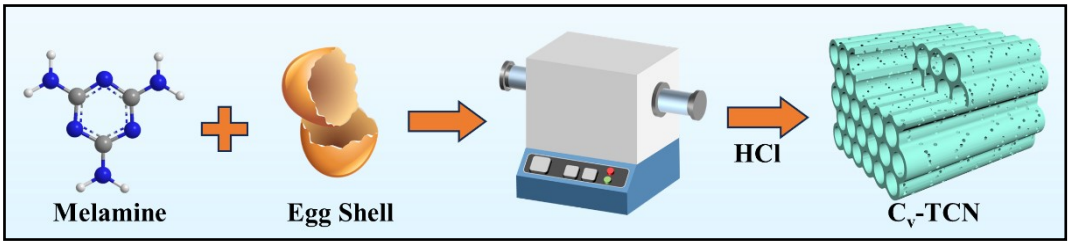

Scheme S1 The schematic diagram of preparing the C_v-TCN samples.

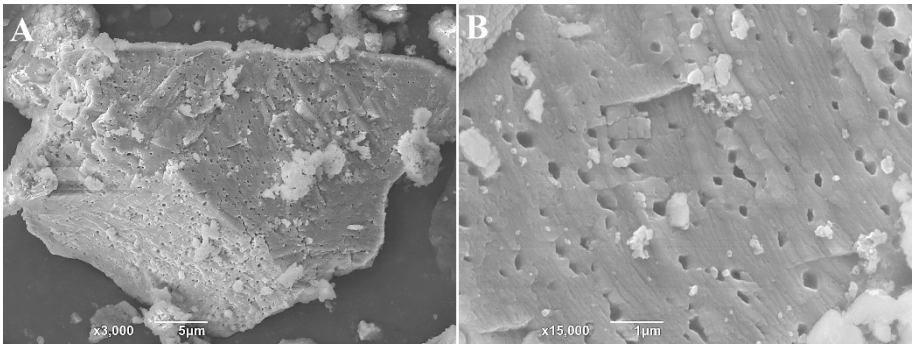

Fig. S1 The SEM images of the eggshell template agent.

Additional discussion

Fig. S1A-B shows the typical SEM images of eggshell. It displays that the densely distributed pores are clearly observed, providing a natural template for the synthesis of porous nanostructures.

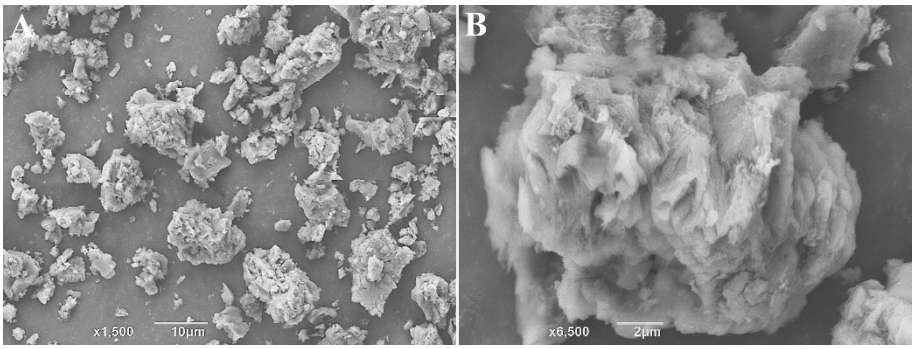

Fig. S2 The SEM images of the prepared pristine bulk carbon nitride (BCN).

Additional discussion

Fig. S2 shows a typical SEM image of a bulk carbon nitride material. It is clear from the image that the irregularly shaped carbon nitride blocks are randomly stacked and distributed across the field of view with no obvious pore structure. This heterogeneous stacked structure usually prevents the efficient transfer of photogenerated charge, leading to lower photocatalytic activity.

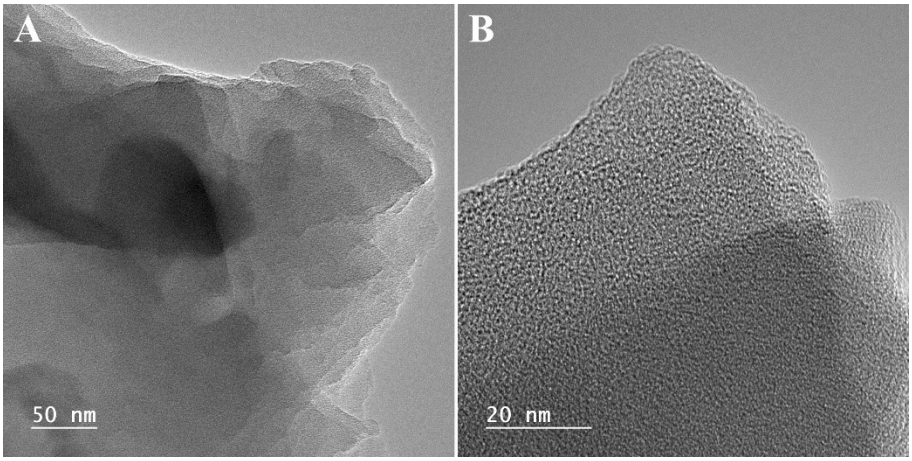

Fig. S3 The TEM (A) and HRTEM (B) images of the prepared pristine bulk carbon nitride (BCN).

Additional discussion

Fig. S3A shows the TEM image of the prepared bulk carbon nitride material. The results show that several carbon nitride nanosheets have been stacked in a disordered manner to form a thicker block, which is in agreement with the SEM results. In addition, the HRTEM results show an amorphous structure as no lattice stripes could be distinguished (Fig. S3B).

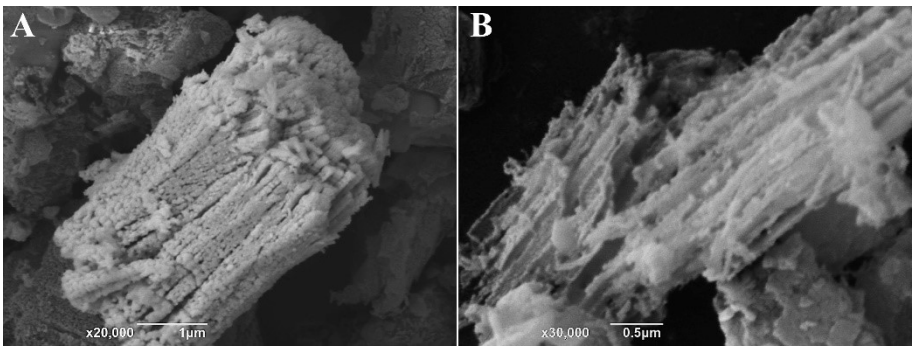

Fig. S4 The SEM images of prepared C_v-TCN.

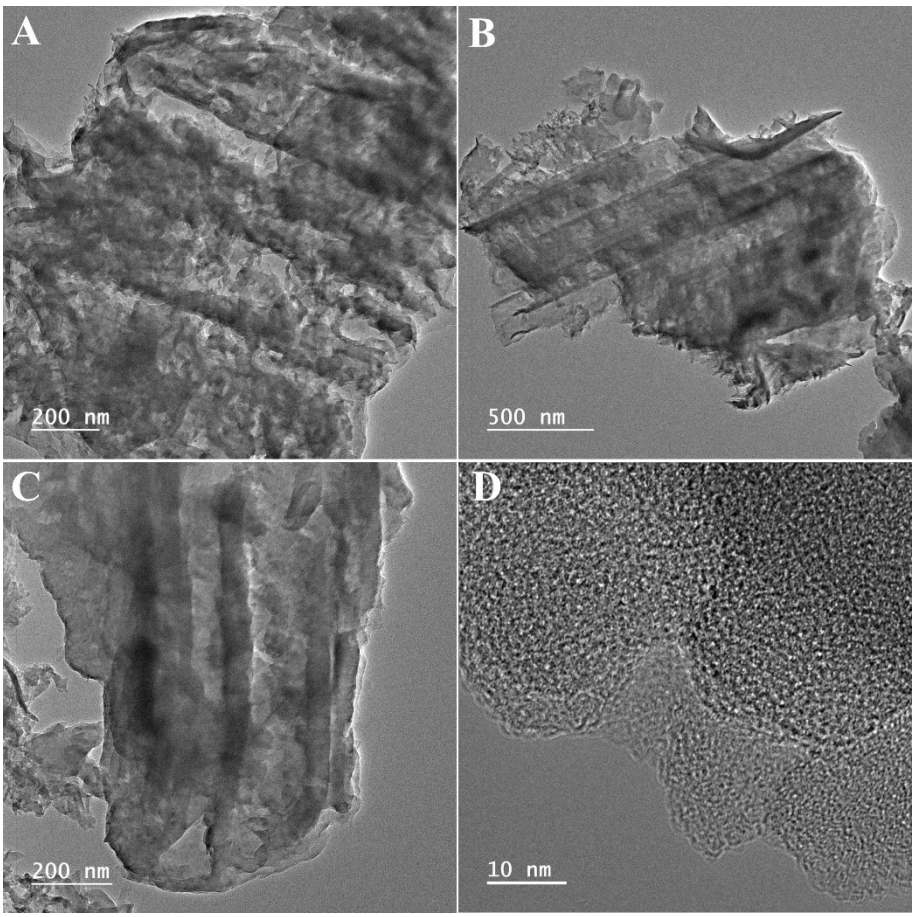

Fig. S5 The TEM and HRTEM images of C_v-TCN samples.

Additional discussion

Fig. S4A shows the SEM image of the prepared carbon nitride nanotubes, where it can be clearly seen that several nanotubes are neatly aligned, which is caused by the pores of the templating agent. Furthermore, the SEM image of the torn nanotubes shows that the nanotubes are hollow (Fig. S4B), which facilitates the transport of light, reactants and products. As shown in Fig. S5, the regular hollow nanotube structure was also confirmed by the TEM results. The TEM images clearly show multiple hollow and open nanotubes arranged together, while no obvious lattice stripes were observed in the HRTEM images.

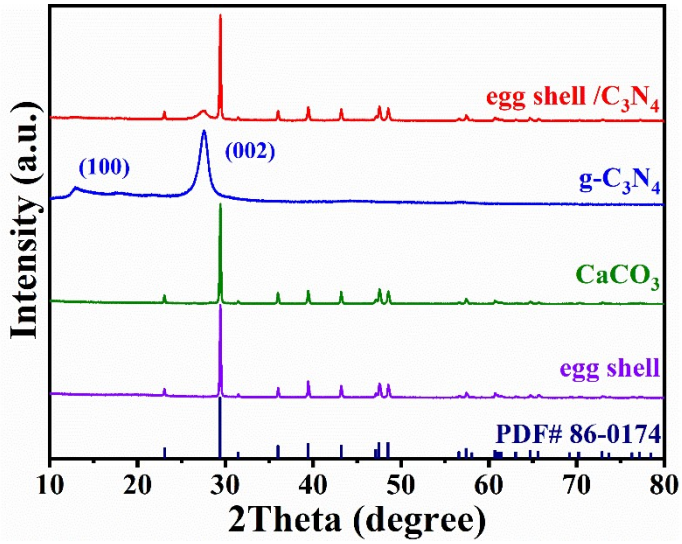

Fig. S6 The XRD pattern of eggshell, $CaCO_3$, g-C_3N_4 and eggshell/C_3N_4 samples.

Additional discussion

Fig. S6 shows that the XRD spectra of the eggshell templating agent and calcium carbonate are almost identical and can be indexed as PDF cards numbered #86-0174. This allows the templating agent to be easily etched away by the acid in the subsequent process. Additionally, the eggshell/C_3N_4 samples after calcination exhibit obvious diffraction peaks of eggshell, (002) and (100) planes of carbon nitride, indicating successful preparation of carbon nitride using eggshell as a templating agent.

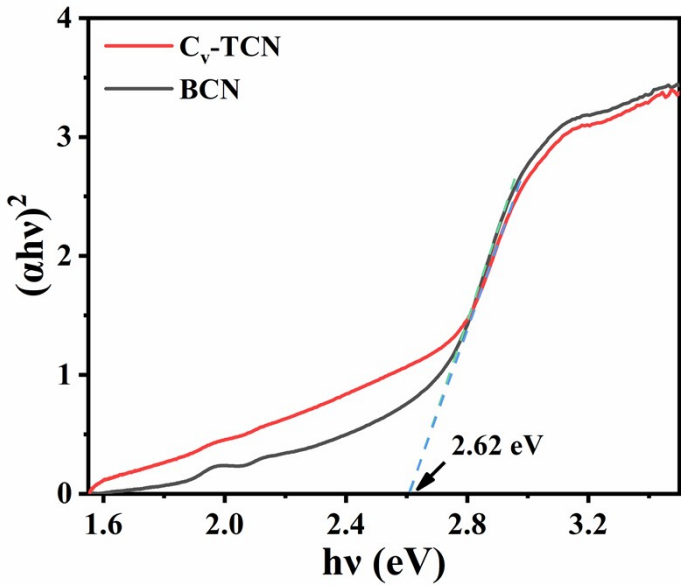

Fig. S7 The Tauc plots of BCN and C_v-TCN samples calculated from UV-Vis curves.

Additional discussion

Fig. S7 shows the Tauc plots obtained from the UV-Vis spectra. It is evident that semiconductors C_v-TCN and BCN have almost identical energy band gaps, corresponding to an optical absorption band edge of approximately 470 nm. However, the curve of C_v-TCN is higher than that of BCN in the range of 2.0-2.7 eV, indicating that C_v-TCN has a better optical response due to multiple reflections of light from its tubular structure.

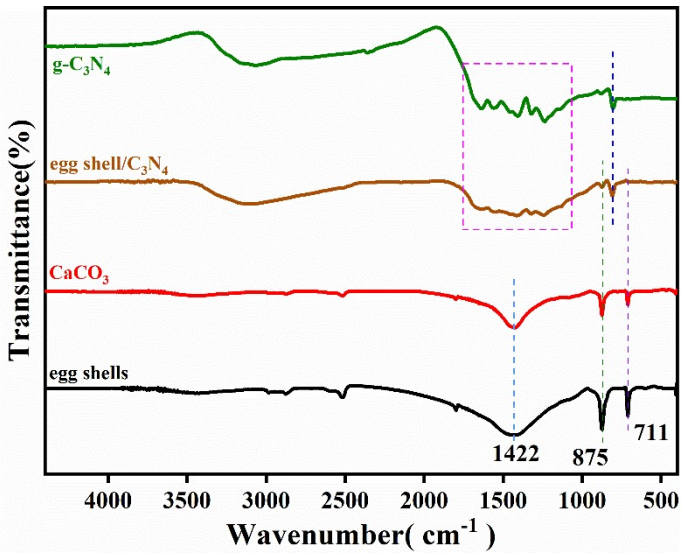

Fig. S8 The FT-IR spectra of prepared eggshells, $CaCO_3$, eggshell/C_3N_4 and g-C_3N_4 samples.

Additional discussion

Fig. S8 displays the FT-IR spectra of the various stages of C_v-TCN sample preparation. The peaks at 1422, 875, and 711 cm^{-1} correspond to the characteristic absorption of the C-O bond antisymmetric stretching vibration, the CO_3^{2-} out-of-plane deformation vibration, and the O-C-O in-plane deformation vibration, respectively. These peaks can be attributed to the $CaCO_3$ species.[3] Furthermore, peaks with wavenumbers ranging from 1100 to 1700 cm^{-1} could be identified as the infrared absorption peaks of C=N and C-N in carbon nitride species.[4] In conclusion, the FT-IR spectra provide additional evidence that carbon nitride nanotubes were successfully fabricated.

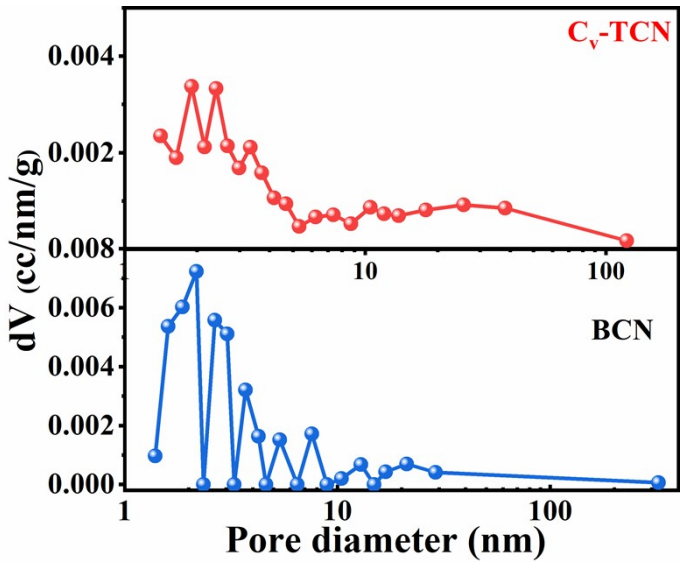

Fig. S9 The pore size distribution curves of C_v-TCN and BCN samples calculated from the N_2 adsorption-desorption results.

Additional discussion

The catalyst's pore size distribution was determined by analyzing the N_2 adsorption-desorption results, as illustrated in Fig. S9. The C_v-TCN sample exhibits a continuous pore size distribution in the 0-10 nm range with an average diameter of 24.36 nm, which is attributed to its porous structure. Furthermore, the pore distribution profile of the C_v-TCN sample displays a bump in the 20-110 nm range, which corresponds to the diameter size of the nanotubes and can be attributed to their contribution. The porous nanotube structure could provide a larger surface area for photocatalyst H_2 evolution reactions.

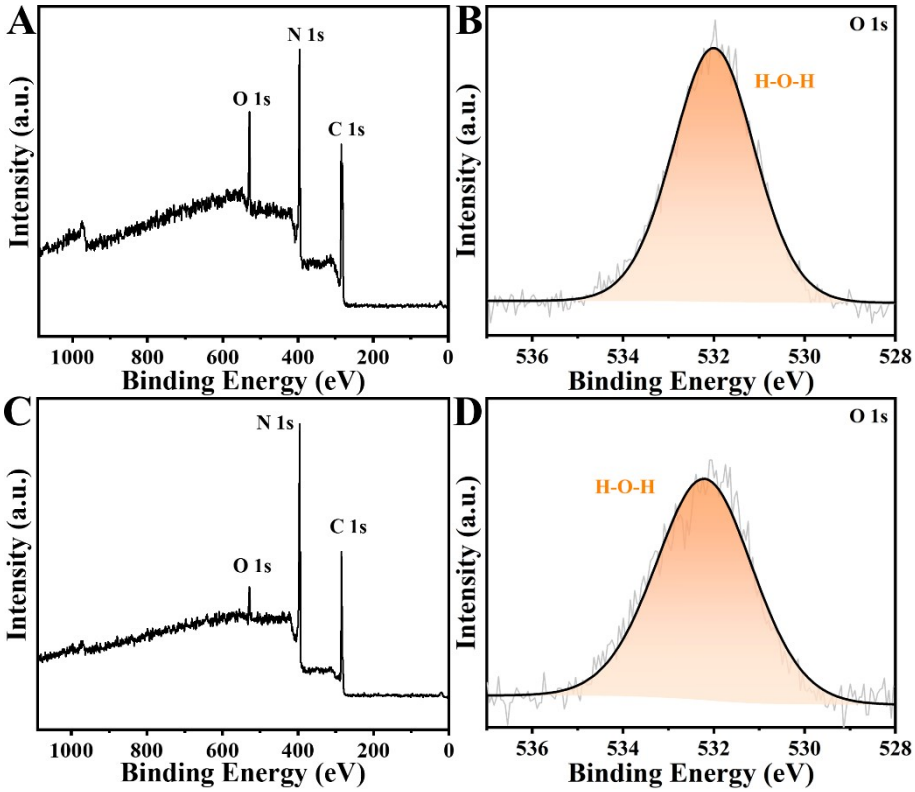

Fig. S10 The survey (A, C) and O 1s high-resolution XPS spectra (B, D) of C_v-TCN (A-B) and BCN (C-D) samples.

Additional discussion

As shown in Fig. S10A and C, the XPS spectra of C_v-TCN and BCN can clearly identify the three peaks of C, N and O, and their fine O 1s spectra could be attributed to adsorbed water molecules. It is noteworthy that the O 1s intensity of the C_v-TCN is significantly higher than that of BCN, indicating that more water molecules were adsorbed on the surface of C_v-TCN, which also reflects the better hydrophilicity of the C_v-TCN catalyst.

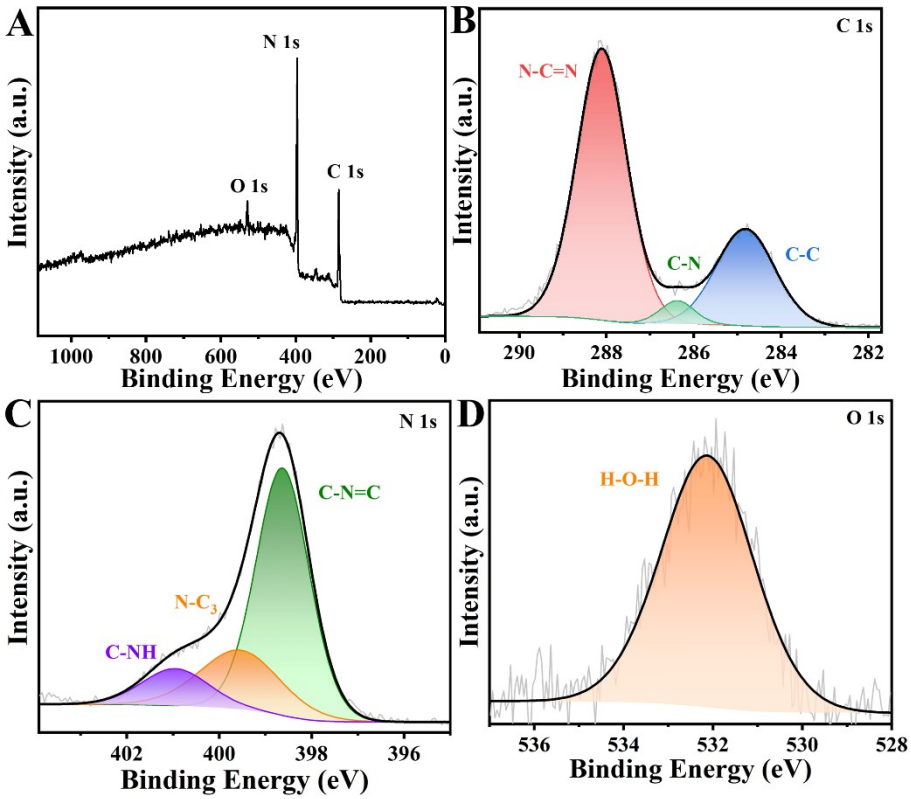

Fig. S11 (A) The survey, C1s, N 1s, and O1s high-resolution XPS spectra of C_v-TCN after the carbon vacancies were repaired.

Additional discussion

To further investigate the significance of carbon vacancies, C_v-TCN powder was immersed in a 0.1 M urea solution for 12 h. The powder was then centrifuged, dried, and calcined in an Ar atmosphere at 550 °C for 1 h to repair some of the carbon defect sites in C_v-TCN. Fig. S11 shows the XPS spectra of the C_v-TCN sample after the carbon vacancies have been filled. The results showed that the main components of the treated samples were C, N and O, and the fine spectra of C 1s and N 1s could be deconvoluted into N-C=N, C-N, C-C, C-N=C, N-C_3 and C-NH_x, respectively, which were similar to those before being repaired. However, there was a significant change in their peak area ratio, as shown in Table S4, the content of -NH_x increased significantly while the content of C-N=C and N-C_3 decreased significantly, and the N/C atom ratio of the

sample also decreased, suggesting that some of the suspended N atoms in the C_v-TCN frame were re-immobilized into the backbone structure due to the additional introduction of carbon atoms at the carbon defect site.

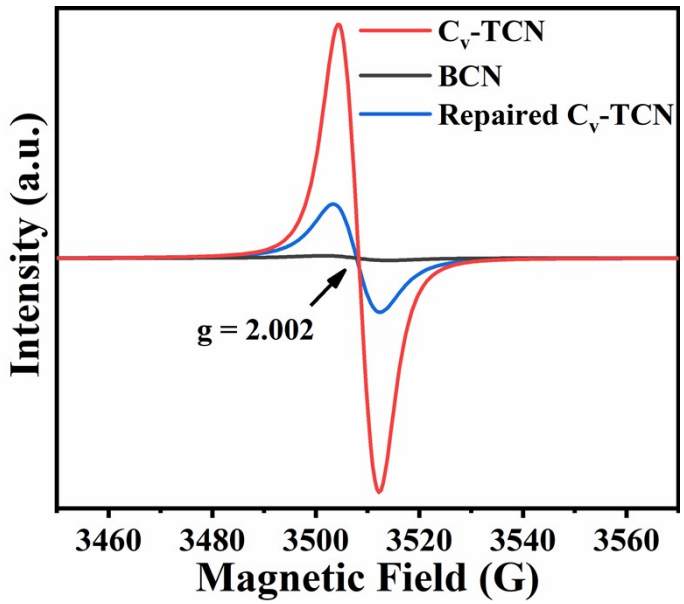

Fig. S12 The ESR spectra of BCN and C_v-TCN samples before and after the carbon vacancies were repaired.

Additional discussion

To confirm that the carbon vacancies were filled, the treated samples underwent EPR testing to probe their lone-pair electron signals. Fig. S12 shows that the EPR signal intensity of the C_v-TCN samples decreased significantly after the treatment, which confirmed that the carbon defective sites in C_v-TCN were filled and the concentration of carbon vacancies was reduced.[5]

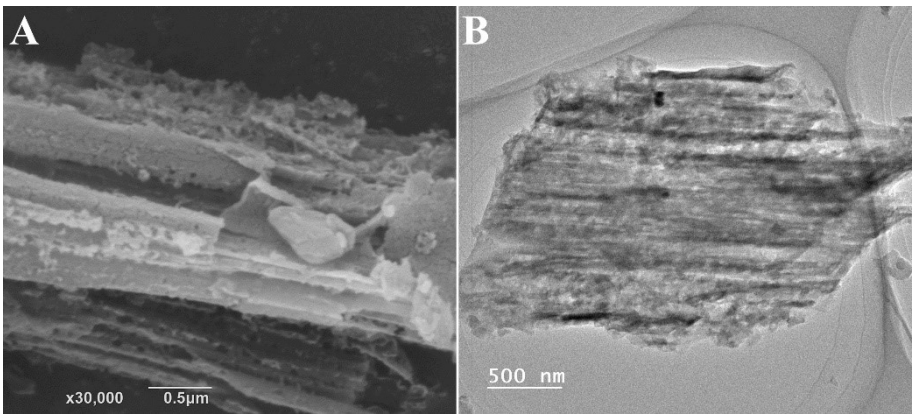

Fig. S13 The SEM (A) and TEM (B) images of C_v-TCN samples after the carbon vacancies were repaired.

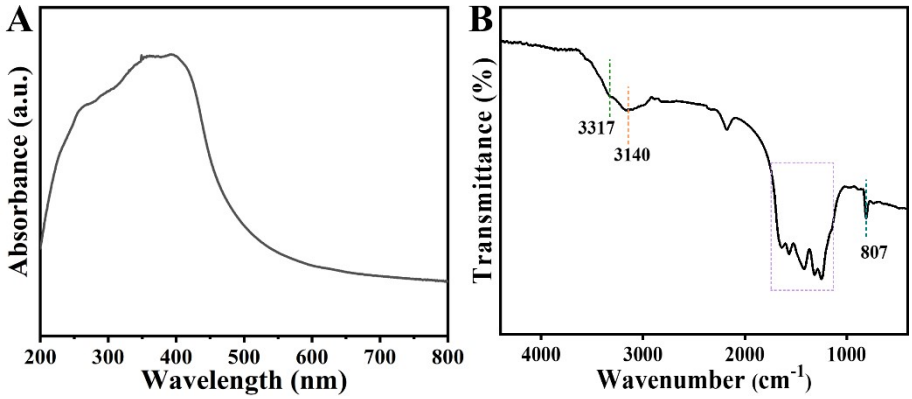

Fig. S14 The UV-Vis diffuse reflectance spectrum (A) and FT-IR spectrum (B) of C_v-TCN samples after the carbon vacancies were repaired.

Additional discussion

Fig. S13 shows the SEM and TEM images of the repaired C_v-TCN sample, indicating the C_v-TCN sample still retains a hollow porous tubular structure. Similarly, as can be seen from Fig. S14, there is no significant change in the optical absorption band edge and FT-IR spectra of the C_v-TCN sample after the carbon vacancies being repaired. This indicates that the reparation of carbon vacancies does not significantly change the characteristic structure and optical properties of C_v-TCN samples.

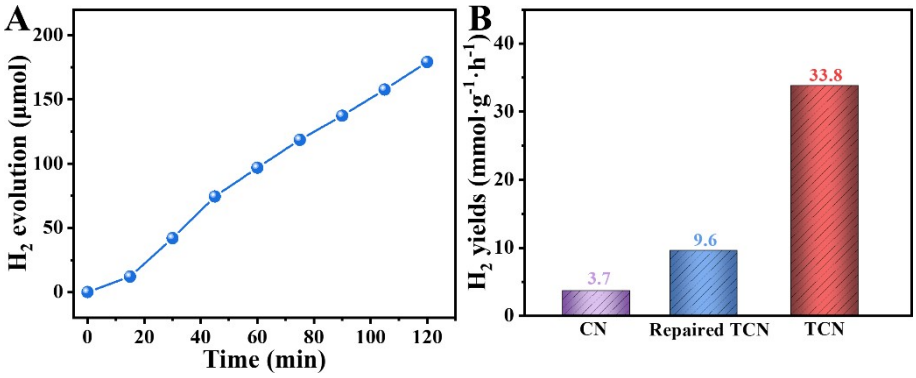

Fig. S15 (A) The photocatalytic H_2 evolution of the C_v-TCN sample after the carbon vacancies being repaired. (B) Comparison of photocatalytic hydrogen evolution rates of BCN and C_v-TCN before and after the carbon vacancies being repaired.

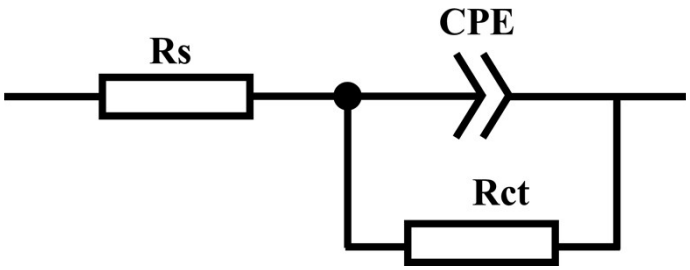

Fig. S16 The simplified equivalent circuit model used to fit the EIS plots.

Additional discussion

R_s represents the solution resistance in the electrochemical cell, R_{ct} represents the resistance in the charge transfer process for the electrode, and the constant phase element (CPE) represents the capacitance of the space charge depletion region at the surface of the electrode. [6-8]

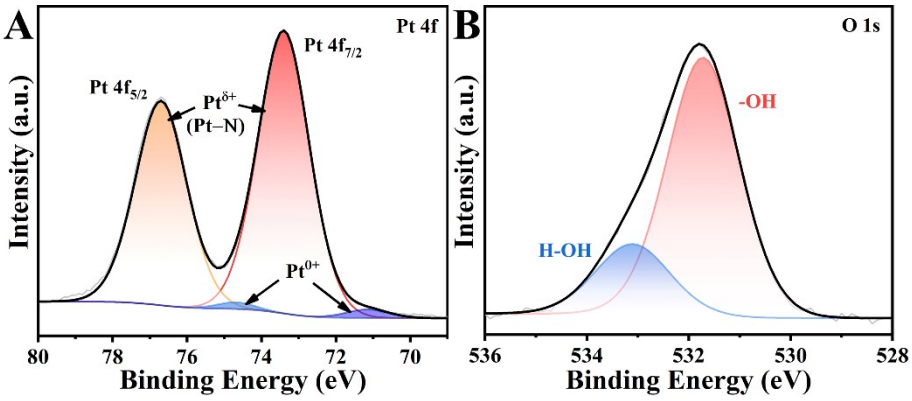

Figure S17 The Pt 4f (A) and O 1s (B) high-resolution XPS spectra of the C_v-TCN sample after photo-depositing the Pt cocatalyst.

Additional discussion

To further verify the formation of chemical bonds between the suspended N atoms and the Pt species, the C_v-TCN samples were subjected to XPS analysis after photo-deposition of Pt, and the results are shown in Figure S17. In particular, in order to ensure the strength of the XPS signal, the amount of Pt added has been increased by a factor of 3. As can be seen from Figure S17A, the Pt 4f orbital is split into Pt $4f_{7/2}$ and Pt $4f_{5/2}$, and can be reasonably deconvoluted into Pt^0 and $Pt^{\delta+}$ species. This indicates that Pt not only forms Pt-Pt bonds with itself but also forms chemical bonds with other atoms. In addition, considering that only the peaks of -OH and adsorbed water were observed in the O 1s high-resolution spectra, no signal for any Pt-O (usually located around the binding energy of 530 eV) was detected. Therefore, combined with the literature, $Pt^{\delta+}$ species can be reasonably attributed to the formed Pt-N bonds. [2, 9-10]

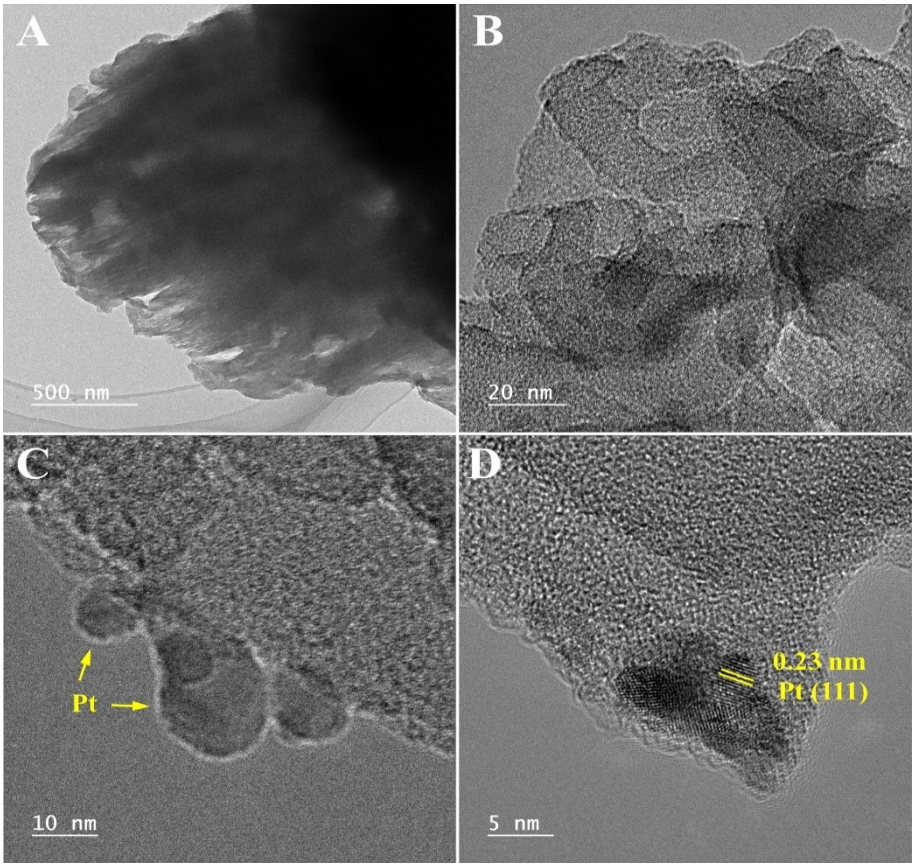

Figure S18 The TEM images of C_v-TCN photocatalyst after the cyclic testing.

Additional discussion

The microscopic topography structure of the C_v-TCN catalyst after cyclic testing has been observed by TEM, and the results are shown in Fig. S18. The TEM images show that the C_v-TCN maintains its nanotube morphology. The lattice fringes with a spacing of 0.23 nm can be clearly observed and belong to the (111) plane of the cocatalyst Pt, which was obtained by the photo-deposition process before the photocatalytic hydrogen evolution reaction. However, the nanotube edges appear blurred in the high-resolution HR-TEM images, which may be due to the photocatalyst self-corrosion.

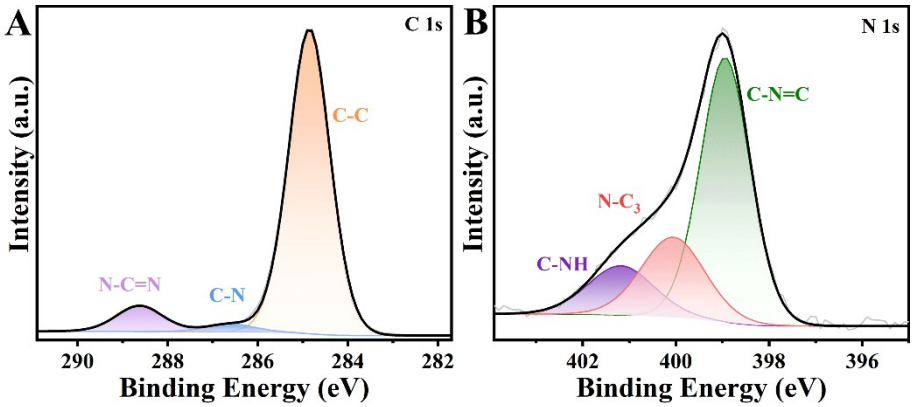

Figure S19 The C 1s (A) and N 1s (B) high-resolution XPS spectra of C_v-TCN sample after photo-depositing Pt species.

Additional discussion

Figure S19 shows the XPS spectra of C_v-TCN catalysts after cyclic testing. As can be seen from the XPS results, the high-resolution C 1s spectra can be deconvoluted into N-C=N, C-N and C-C peaks. Similarly, the high-resolution N 1s spectra can be fitted into the three bonds of C-NH_x, N-C_3 and C-N=C. This is not much different from that before the test, indicating that the C_v-TCN sample has good stability.

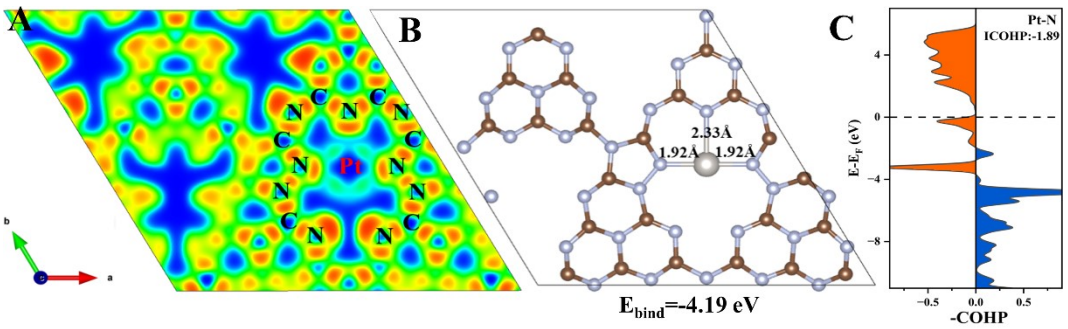

Figure S20 The DFT calculated results of the electron cloud distribution for C_v-TCN catalyst after loading of Pt cocatalyst (A), the corresponding length of Pt-N bonds (B) and crystal orbital Hamilton population between Pt and N atoms (C).

Additional discussion

The DFT theory was used to verify the strong interaction between the suspended N atoms and the Pt species. As shown in Figure S20A, the electron localization function (ELF) diagrams for C_v-TCN catalyst after loading of Pt indict that there is significant electron sharing between the suspended N atoms and the Pt atoms, meaning the chemical bond was formed between Pt and N atoms,[11] and the length of it were calculated to be 1.92 and 2.32 Å (Figure S20B). It is worth noting that the E_{bind} value was calculated as -4.19 (much less than 0), indicating the good stability of the formed Pt-N bonds. Moreover, the crystal orbital Hamilton population (COHP) was introduced to further explain the bonding interaction between N and Pt. As shown in Figure S20C, the bonding states (blue) exist below E_F, which further confirms the formation of the Pt-N bonds. [12-13]

3. Supplemental Tables

Table S1 Fitting results of the Nyquist plots of BCN and C_v-TCN samples in Figure 2E.

Sample	Rs (Ω)	Rct (Ω)	CPE (F)
C_v-TCN	41.94	3.47×10^{5}	1.21×10^{-5}
BCN	41.65	5.26×10^{5}	1.28×10^{-5}

Table S2 Fitting parameters of transient fluorescence kinetics for C_v-TCN and BCN samples.

	t_1 (ns)	t_2 (ns)	A1	A2	t_{ave} (ns)
C_v-TCN	44.38	1.17	121.5	20896	8.698
BCN	2.118	0.637	4202	35310	1.057

Table S3 The content of each element of BCN, C_v-TCN samples before and after the carbon vacancies being repaired, calculated by XPS results.

Sample	C (%)	N (%)	O (%)	N/C
C_v-TCN	39.18	49.37	11.45	1.26
BCN	44.96	48.87	6.17	1.09
Repaired C_v-TCN	44.21	49.61	6.18	1.12

Table S4 The proportion of each fitted peak of the XPS spectra in Figure 4.

Sample	N-C=N (%)	CN-H_x (%)	C-C (%)	C-N=C (%)	N-C_3 (%)	-NH_x (%)
C_v-TCN	74.33	6.35	19.20	62.55	22.55	14.90
BCN	76.79	3.69	19.52	68.07	23.49	8.44
Repaired C_v-TCN	67.78	3.98	28.24	64.71	23.14	12.15

Table S5 The comparison of photocatalytic H_2 evolution performance of carbon nitride catalysts similar to C_v-TCN.

Photocatalysts	Cocatalyst	Light source	Sacrificial agent (mL%)	H_2 yield ($\mu mol \cdot g^{-1} \cdot h^{-1}$)	Ref.
C_3N_4 nanotubes	3 w% Pt	300 W Xe lamp >420 nm	10 % TEOA	8600	*13*
Disordered nitrogen-defect porous C_3N_4	3 w% Pt	300 W Xe lamp >420 nm	10 % TEOA	7026	*14*
N-deficient C_3N_4 bunchy tubes	3 w% Pt	300 W Xe lamp >420 nm	10 % TEOA	819	*15*
C defective C_3N_4 tubes	1 w% Pt	300 W Xe lamp >350 nm	10 % TEOA	6588.1	*16*
C_3N_4 horn-like tubes	1 w% Pt	300 W Xe lamp >420 nm	10 % TEOA	1354	*17*
N-deficient C_3N_4	1 w% Pt	300 W Xe lamp >420 nm	10 % Methanol	5450	*18*
N-deficient C_3N_4	Pt	300 W Xe lamp >420 nm	20 % TEOA	2015.5	*19*

Nitrogen defects and few-layer nanosheet	3 w% Pt	300 W Xe lamp >420 nm	10 % TEOA	5375	*20*
N/C-deficient C_3N_4	3 w% Pt	300 W Xe lamp >420 nm	10 % TEOA	1271	*21*
Carbon vacancies and oxygen doped C_3N_4	3 w% Pt	300 W Xe lamp >350 nm	10 % TEOA	7414	*22*
N vacancy modified C_3N_4 nanosheets	3 w% Pt	300 W Xe lamp >420 nm	10 % TEOA	5740	*23*
N-vacancy and C-doped C_3N_4	5 w% Pt	300 W Xe lamp >420 nm	---	27600	*24*
N-vacancy and S-doped C_3N_4	1 w% Pt	300 W Xe lamp >300 nm	10 % TEOA	4219.9	*25*
Carbon vacancies modified C_3N_4 tubes	3 w% Pt	300 W Xe lamp >300 nm	10 % Methanol	33800	***This Work***

4. Supplemental References

1. S. Cao, J. Low, J. Yu and M. Jaroniec, *Adv. Mater.*, 2015, **27**, 2150-2176.
2. L. Zhang, R. Long, Y. Zhang, D. Duan, Y. Xiong, Y. Zhang and Y. Bi, *Angew. Chem.*, 2020, **132**, 6283-6288.
3. K. Zhang, W. Yang, F. Ge, B. Xu, Y. Chen, X. Yin, Y. Liu and H. Zuo, *Int. J. Biol. Macromol.*, 2020, **151**, 691-701.
4. X. Yang, F. Qian, G. Zou, M. Li, J. Lu, Y. Li and M. Bao, *Appl. Catal. B-Environ.*, 2016, **193**, 22-35.
5. X. Wang, J. Meng, X. Zhang, Y. Liu, M. Ren, Y. Yang and Y. Guo, *Adv. Funct. Mater.*, 2021, **31**, 2010763.
6. B. Sun, H. Li, H. Yu, D. Qian and M. Chen, *Carbon*, 2017, **117**, 1-11.
7. J. Lu, Y. Wang, J. Huang, L. Cao, J. Li, G. Hai and Z. Bai, *Mat. Sci. Eng. B*, 2016, **214**, 19-25.
8. N. Tian, H. Huang, C. Liu, F. Dong, T. Zhang, X. Du, S. Yu and Y. Zhang, *J. Mater. Chem. A*, 2015, **3**, 17120-17129.
9. E. Cui, Y. Lu, Z. Li, J. Sang, Z. Wang, M. Xie, X. Yang, J. Cao and Y. Zhang, *Appl. Catal. B-Environ.*, 2024, **347**, 123806.
10. Y. Hu, Y. Qu, Y. Zhou, Z. Wang, H. Wang, B. Yang, Z. Yu and Y. Wu, *Chem. Eng. J.*, 2021, **412**, 128749.
11. S. -L. Li, Q. Li, Y. Chen, Y. Zhao and L. -Y. Gan, *Appl. Surf. Sci.*, 2022, **605**, 154828.
12. S. -L. Li, H. Yin, X. Kan, L. Y. Gan, U. Schwingenschlogl and Y. Zhao, *Phys. Chem. Chem. Phys.*, 2017, **19**, 30069-30077.
13. X. Yu, C. Hu, D. Hao, G. Liu, R. Xu, X. Zhu, X. Yu, Y. Ma and L. Ma, *Sol. RRL*, 2021, **5**, 2000827.
14. C. Cheng, J. Shi, L. Wen, C. -L. Dong, Y. -C. Huang, Y. Zhang, S. Zong, Z. Diao, S. Shen and L. Guo, *Carbon*, 2021, **181**, 193-203.
15. G. Ge, X. Guo, C. Song and Z. Zhao, *ACS Appl. Mater. Inter.*, 2018, **10**, 18746.

16. B. Yang, H. Han, Q. Zhang, G. Liao, W. Cheng, G. Ge, J. Liu, X. Yang and R. Wang, *Carbon*, 2023, **202**, 348-357.

17. C. Liu, H. Huang, L. Ye, S. Yu, N. Tian, X. Du, T. Zhang and Y. Zhang, *Nano Energy*, 2017, **41**, 738.

18. Y. Liu, W. Yin, Q. Lin, Z. Li, Q. Zhong and B. Fang, *Appl. Surf. Sci.*, 2023, **640**, 158386.

19. J. Liu, W. Fang, Z. Wei, Z. Qin, Z. Jiang and W. Shangguan, *Appl. Catal. B-Environ.*, 2018, **238**, 465.

20. Q. Shen, N. Li, R. Bibi, N. Richard, M. Liu, J. Zhou and D. Jing, *Appl. Surf. Sci.*, 2020, **529**, 147104.

21. X. Wang, L. Wu, Z. Wang, H. Wu, X. Zhou, H. Ma, H. Zhong, Z. Xing, G. Cai, C. Jiang and F. Ren, *Sol. RRL*, 2019, **3**, 1800298.

22. B. Yang, X. Li, Q. Zhang, X. Yang, J. Wan, G. Liao, J. Zhao, R. Wang, J. Liu, R. D. Rodriguez and X. Jia, *Appl. Catal. B-Environ.*, 2022, **314**, 465.

23. Y. Zhang, Z. Huang, C. -L. Dong, J. Shi, C. Cheng, X. Guan, S. Zong, B. Luo, Z. Cheng, D. Wei, Y. Huang, S. Shen and L. Guo, *Chem. Eng. J.*, 2022, **431**, 134101.

24. J. Hou, M. Yang, Q. Dou, Q. Chen, X. Wang, C. Hu and R. Paul, *Chem. Eng. J.*, 2022, **450**, 138425.

25. S. Hou, X. Gao, S. Wang, X. Yu, J. Liao and D. Su, *Small*, 2024, 2302500.